Enhancement of photo-electrochemical reactions in MAPbI₃/Au

Shenghuang Lin[1,†], Yang Liu[1,†], Zhixin Hu[2,†], Gongxun Bai[1], Yanyong Li[1], Huiyu Yuan[1],

Yunzhou Xue[1], Lukas Rogée[1], Jianhua Hao[1], Xuming Zhang[1,*], Shu Ping Lau[1,*]

[1] Department of Applied Physics, The Hong Kong Polytechnic University, Hung Hom,

Hong Kong SAR, P. R. China

[2] Center for Joint Quantum Studies, Physics Department of Tianjin University, Tianjin,

P. R. China

[†]These authors contributed equally to this work.

[*] Address correspondence to apsplau@polyu.edu.hk and xuming.zhang@polyu.edu.hk

Keywords: Perovskite, photo-electrochemical reaction, atmospheric pressure physical vapor deposition

Abstract:

Methylammonium lead iodide perovskite (MAPbI$_3$), as a new type of light absorber for optoelectronic devices, has attracted much interest and served as foundation for new device concepts. However, most studies to date are mainly focusing on the fabrication of MAPbI$_3$-based solar cells and photodetectors. Here we report a facile method to prepare a large-scale MAPbI$_3$ photocatalyst through atmospheric pressure physical vapor deposition. The photocurrent density of the MAPbI$_3$ coated with an Au layer can reach 30.8 and 85.5 μA/cm^2 in ethanol and H$_2$SO$_4$ electrolytes, respectively. Meanwhile, the strong interaction between H$_2$O orbitals and the conduction band of MAPbI$_3$ is revealed by density functional theory calculations. Our study opens a new pathway for the development of perovskite-based photo-electrochemical reaction systems.

1. Introduction

Searching for a new type of clean, renewable, cheap and safe energy source to partly or completely replace fossil fuels and nuclear energy has been one of the most important issues in modern society and will be for our future world. Recently, hydrogen, potentially as a next-generation energy carrier, has received considerable attention around the world. It has been revealed that using inexhaustible sunlight for photocatalytic water splitting is a good method for hydrogen production. Therefore, one key issue is to seek for potential materials to enhance the photo-electrochemical reaction (PECR) during the process of water splitting. Up to now, TiO_2 compounds are mainly used for UV light absorption when serving as catalysts for PECR because of their wide bandgap[1]. One purpose for seeking new type of photocatalysts with small bandgap to absorb visible light is of great importance. Recently, hybrid organic-inorganic perovskites in the formula of ABX_3 (A = $CH_3NH_3^+$; B = Pb^{2+} or Sn^{2+}; and X = Cl^-, I^-, and/or Br^-) have been intensively studied as high performance light absorbers in thin-film solar cells for solar energy harvesting [2-12]. Such light absorbers with small bandgaps show potential applications for photocatalysis when using visible light (solar energy) as renewable source. Thus, the preparation of large-scale and high-quality perovskite thin films is of great interest. Over the past few years, significant efforts have been employed to increase the grain size of lead halide perovskite for high performance solar cells by solution process [13, 14] or high-vacuum physical vapor deposition (HVPVD) [7, 15-16] method. It is reported that the tetragonal phase methylammonium lead halide perovskites (MAPbI$_3$ or $CH_3NH_3PbI_3$) are stable only at

specific I^- and H^+ concentrations ($[I^-] \leqslant [H^+]$, pH $\leqslant -0.5$, and $-\log[I^-] \leqslant -0.4$), and the solar HI (hydrogen iodide) splitting efficiency of MAPbI$_3$ could be as high as ~0.81% when using Pt as a co-catalyst [17]. Since then, little has been done in the field. Here we demonstrate that MAPbI$_3$ crystals can be controllably grown via atmospheric pressure physical vapor deposition (APPVD), which is different from the previously reported methods needing high vacuum level [15, 16, 18]. Meanwhile, the APPVD deposited MAPbI$_3$ crystals covered by a gold (Au) film exhibited an enhanced PECR, offering a new material platform for the fundamental investigation of the optical and photocatalytic properties of perovskite-based system.

2. Results and discussion

2.1 Preparation and Characterizations of MAPbI$_3$

Figure 1a shows the optical image of the PbI$_2$ crystals grown on FTO substrate. Figures 1b and Figures S2a, b show the scanning electron microscopy (SEM) photographs of the hexagonal-shaped PbI$_2$ microplates and some of them are stacked on each other. Figure 1c shows the magnified TEM image of a PbI$_2$ micropate with an edge length of ~300 nm. The top inset in Figure 1c presents the selected area electron diffraction (SAED) pattern with a six-fold symmetry, revealing the high crystalline quality of the PbI$_2$ with five distinguishing yellow arrows assigned to (0 1 $\bar{1}$ 0), (1 0 $\bar{1}$ 0), (1 $\bar{1}$ 0 0), (1 $\bar{2}$ 1 0) and (2 $\bar{1}$ $\bar{1}$ 0) planes with lattice spacing of 0.40, 0.46, 0.38, 0.21 and 0.24 nm, respectively. The bottom inset in Figure 1c reveals the crystal plane spacing of ~0.21 nm, which corresponds to the (1 $\bar{2}$ 1 0) crystal plane as described previously. Three vibrational modes of E^1_2 (68 cm^{-1}), A^1_1 (101 cm^{-1}) and A^2_1

(138 cm^{-1}) can be observed in the Raman spectrum as shown in Figure 1d. The peak at 101 cm^{-1} is assigned to the bending and stretching of Pb–I bonds, corresponding to the diagnostic mode of the inorganic cages [26]. The PL position located at 512 nm (Figure 1e) is the characteristic of PbI_2 [16]. As for the XRD pattern of the PbI_2 microplates as shown in Figure 1f, the peaks at $2\theta = 12.6°$, $25.5°$, $38.5°$ and $52.3°$ correspond to the (0 0 6), (0 0 12), (0 0 18) and (0 0 24) planes of PbI_2 (ICDD-PDF: No.73-1754), which also reveal a preferred orientation along the (0 0 6) plane. From the above data, it can be confirmed that the PbI_2 microplates were successfully prepared.

After that, the as-grown PbI_2 crystals were converted into perovskites by reacting with gas-phase methylammonium halides (see Materials and Methods). The converting reaction was carried out in a quartz tube at atmospheric pressure with argon as a protective carrier gas. It should be noted that the conversion of PbI_2 into perovskite by reacting with gas-phase methylammonium halides can prevent the chemical dissolution of PbI_2 and perovskite, and even maintain their morphology and crystalline quality well when compared to the reaction in organic solvents [15].

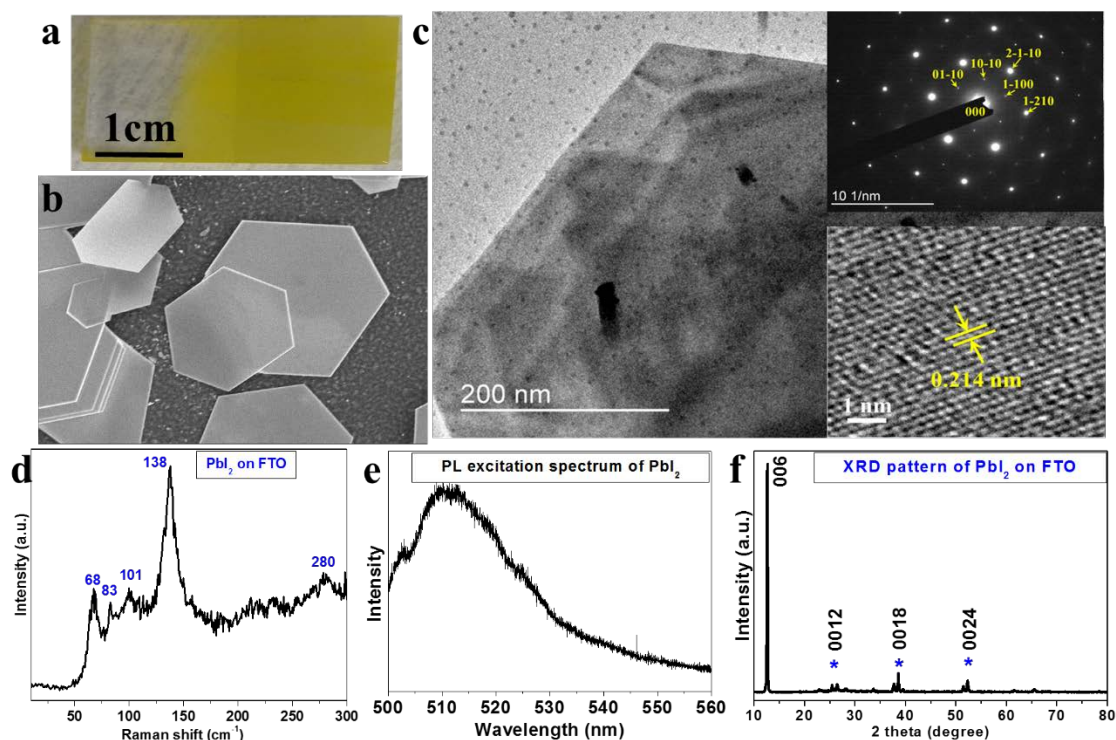Fig. 1. **Growth of large-area PbI₂ microplates on FTO substrate**. (a) Optical image of the PbI₂ crystals. (b) SEM images of the hexagonal PbI₂ microplates. (c) TEM images of the PbI₂ microplate. The insets in (c) reveal the SAED pattern and HRTEM image of the PbI₂ crystal. The HRTEM imaging indicates a highly crystalline PbI₂ with six-fold symmetric diffraction patterns from the SAED pattern. (d)-(f) Raman spectrum, PL spectrum and XRD pattern of the PbI₂ crystals, respectively.

Figure 2a illustrates the crystal structures of the PbI₂ and MAPbI₃. Hexagonal PbI₂ possesses a layered structure where each octahedron shares two equatorial halide atoms and one axial halide atom with its neighbors. MAPbI₃ exhibits a tetragonal structure, and the octahedrons in MAPbI₃ only share one halide atom with their neighbors in both equatorial and axial directions[15]. When the conversion proceeds, the methylammonium group is surrounded by eight octahedrons and the equatorial halide atoms are relocated, revealing the PbI₂ octahedrons are twisted to some extent [15]. Compared with Figure 1a, the colour of the PbI₂ crystals is changed from yellow to black (Figure 2b). Figure 2c

shows the SEM image of the as-prepared perovskite crystals. Many regular hexagonal microplates can be observed (also in Figures S2c and d), revealing the morphologies of the perovskite crystals remain unchanged after the conversion process. Although the crystal structures of the PbI_2 and $MAPbI_3$ are significantly different as shown in Figure 2a, their effective overall morphologies still remain the same to some extent. To further confirm the structural properties of the as-prepared PbI_2 converted samples, we also performed TEM, Raman and PL (photoluminescence) characterizations.
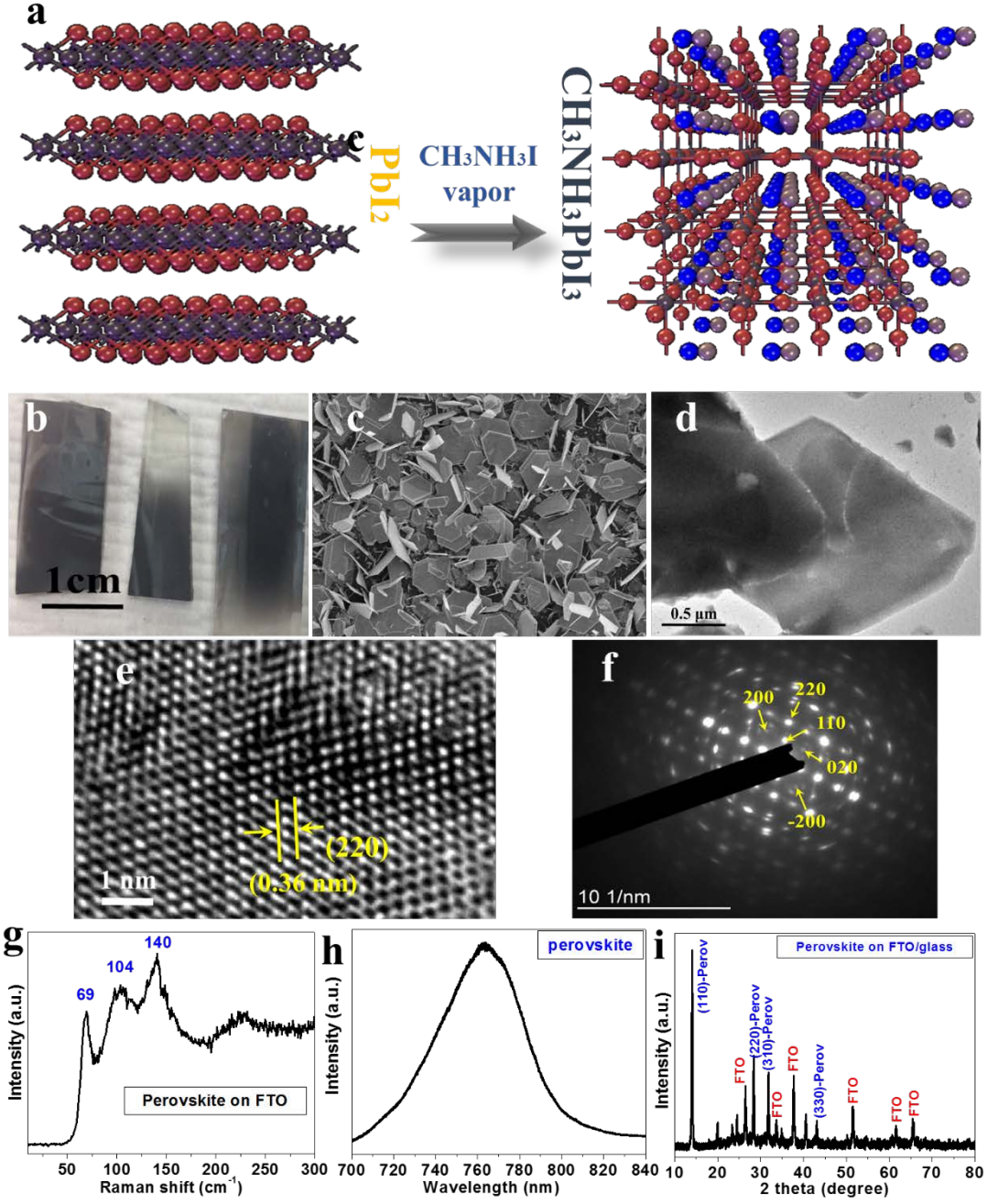
Fig. 2. **Conversion of PbI₂ microplates into perovskite crystals**. (a) Schematic illustration of the lattice

structure changes from layered PbI_2 to perovskite after the reaction with methylammonium iodide. (b)

Optical images of the perovskite on FTO. (c) SEM image of the perovskite microplates. (d)-(e) TEM and

HRTEM images of the studied perovskite microplates. (f) SAED pattern of the perovskite microplates.

(g)-(i) Raman spectrum, PL spectrum and XRD pattern of the perovskite microplates, respectively.

Figure 2d shows a TEM image of a hexagonal perovskite microplate with a size of

~2.5 μm. Figure 2e shows the HRTEM image of the perovskite, the crystal plane spacing of the sample is ~0.36 nm, which corresponds to (2 2 0) crystal plane. Figure 2f shows the SAED pattern of the perovskite with five distinguishing yellow arrows assigned to the (2 0 0), (2 2 0), (1 1 0), (0 2 0) and (-2 0 0) planes with lattice spacing of 0.44, 0.36, 0.70, 0.60 and 0.44 nm, respectively. Three vibrational modes of E^1_2 (69 cm^{-1}), A^1_1 (104 cm^{-1}) and A^2_1 (140 cm^{-1}) can also be found in Figure 2g. The peak at 104 cm^{-1} is also assigned to the bending and stretching of Pb–I bonds, but the broad unstructured 200–300 cm^{-1} feature is assigned to the torsional mode of methylammonium cations [27]. The PL peak position located at ~765 nm (Figure 2h) is assigned to the perovskite [16]. In terms of the XRD pattern as shown in Figure 2i, the peaks at 2θ = 14.1°, 28.4°, 31.9° and 43.1° correspond to the (1 1 0), (2 2 0), (3 1 0) and (3 3 0) planes of tetragonal MAPbI$_3$ [29] with a preferred orientation along the (110) plane, which are in good agreement with the reported results [28]. Fig S3 shows the XRD pattern of the perovskite microplates prepared with different conversion times. At the perovskite conversion stage of 6h, the peaks of the PbI$_2$ microplates showed a similar pattern with the one at the initial stage. The corresponding peaks of 2θ = 12.6° and 14.1° can be found, revealing the coexistence of PbI$_2$ and MAPbI$_3$. When the conversion proceeds with another 4h (with a total conversion time of 10h at this work), the PbI$_2$ crystals are mostly converted into MAPbI$_3$, giving feature peaks similar to those ones as shown in Figure 2i.

In addition, we also measured the thickness of the as-prepared perovskite crystals through AFM (atomic force microscopy). Figure S4 reveals the thickness distribution

of the perovskite crystals after measuring 50 crystals. The thicknesses of the perovskite crystals are ranging from 11 nm to 220 nm, the most frequent thicknesses are between 50 and 90 nm. The average thickness of the perovskite microplates is estimated to be ~80 nm.

2.2 Photo-electrochemical reaction of MAPbI₃

In a typical PECR system, the photocurrent density is a crucial factor to evaluate the generation of electrons under light irradiation and they have a positive correlation. Here we performed the photocurrent measurements of the samples in ethanol under illumination with a Xe lamp with a cut-off filter ($\lambda > 420$ nm). The working system for detecting the photo-electrochemical activity of MAPbI₃ is shown in Figure 3a. Figures 3b and c show the photocurrent density of the MAPbI₃ and MAPbI₃/Au samples as a function of the growth time of PbI₂. It can be found the photocurrent density of MAPbI₃ and MAPbI₃/Au is remarkably increased when the growth time of the PbI₂ samples are increased from 5 h to 20 h and the highest photocurrent density for MAPbI₃ and MAPbI₃/Au can be up to ~ 17.8 $\mu A/cm^2$ and ~30.8 $\mu A/cm^2$ respectively with an applied voltage of -0.5 V. This result indicates that the growth time of the PbI₂ plays a key role in the grain growth and film formation of the MAPbI₃ and it even determines the light absorption performance and photoexcited electron generation of the MAPbI₃ photocatalyst. Namely, the longer the growth time of the PbI₂, the higher photocurrent we got in the MAPbI₃ system. As shown in Figures 3d and e, the MAPbI₃/Au presents a higher photocurrent when compared with the PbI₂ and the bare MAPbI₃. The photocurrents are independent of the applied voltage, which means the MAPbI₃/Au

system revealing better photo-electrochemical performance in ethanol. On the basis of the further results of the UV-vis spectrophotometer measurement as shown in Figure S5a-c, it can be attributed to the fact that the light absorption of the $MAPbI_3$ is broader than that of the PbI_2, which means more generation of electrons on the conduction band of $MAPbI_3$. This is also contributed to the highest photocurrent obtained in the $MAPbI_3$/Au system due to the enhancement of light absorption by the Au film (Figure S5a-c). By comparing the PL decay lifetime of the $MAPbI_3$ with the $MAPbI_3$/Au, the average carrier lifetime in the $MAPbI_3$/Au system is only 29 ns, which is remarkably smaller than that of the $MAPbI_3$ (as high as ~237.9 ns, see Figures S5b & c), revealing the enhancement of carrier recombination at the Au interface of $MAPbI_3$. Namely, the $MAPbI_3$/Au is boosting the light harvest. Meanwhile, the lower lifetime in the $MAPbI_3$/Au also reveals more photo-induced electrons making great contributions to the PECR.
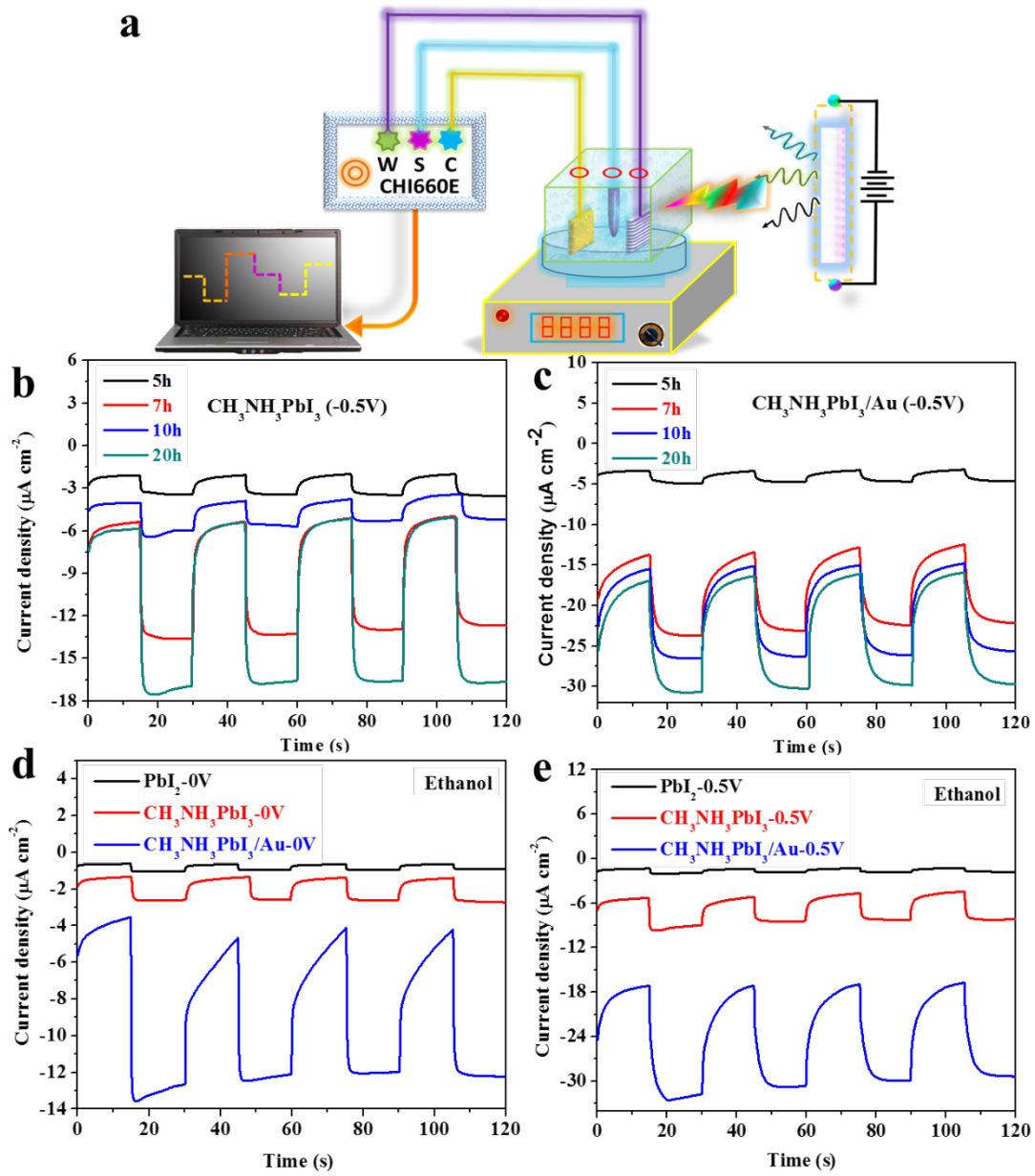
Figure 3. (a) Schematic illustration of the photocatalytic system. W, S and C represent the working, standard and counter electrodes, respectively. (b)-(c) MAPbI$_3$ and MAPbI$_3$/Au with different growth times at an applied voltage of -0.5 V vs. RHE at 100 mW cm^2 in ethanol. (d)-(e) PbI$_2$, MAPbI$_3$ and MAPbI$_3$/Au at an applied voltage of 0 V and -0.5 vs. RHE at 100 mW cm^2 in ethanol.
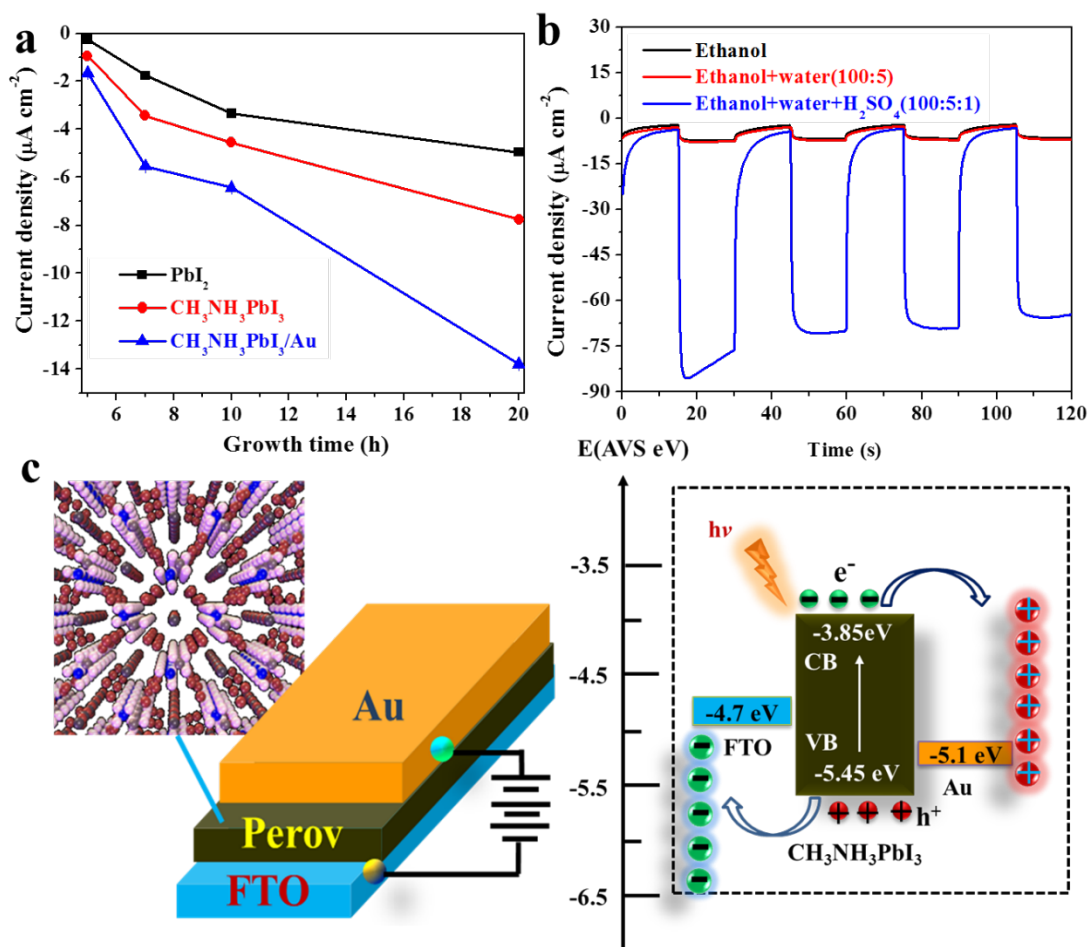
Figure 4. (a) Amperometric I–t curve of the PbI_2, $CH_3NH_3PbI_3$ and $CH_3NH_3PbI_3$/Au with different growth times at an applied voltage of 0 V vs. RHE at 100 mW cm^2 in ethanol. (b) Amperometric I–t curve of $CH_3NH_3PbI_3$/Au at an applied voltage of -0.5 V vs. RHE at 100 mW cm^2 in ethanol, ethanol/H_2O solution and ethanol/H_2SO_4 solution. (c) Schematic illustration of the visible-light excited charge-transferred process for FTO/MAPbI$_3$/Au; here CB = Conduction band, VB = Valence band. -4.7eV and -5.1eV represent the Fermi level of FTO and Au, respectively.

In addition, we also collect the photocurrent density of the PbI_2, MAPbI$_3$ and MAPbI$_3$/Au prepared at different growth times (Figure 4a), which further confirms the results in Figure 3. In order to evaluate the PECR on the MAPbI$_3$/Au, the photocurrent density measurements were carried out in ethanol, ethanol/H_2O solution and ethanol/H_2O/H_2SO_4 solution (Figure 4b). As shown in Figure 3, the photocurrent

13

density of the MAPbI$_3$/Au was stable but low (~7.4 μA/cm^2) in ethanol and ethanol/H$_2$O solution (volume ratio of 100:5). This is owing to the low conductivity and proton concentration of ethanol and ethanol solution. When ethanol and ethanol/H$_2$O solution were replaced by ethanol/H$_2$O/H$_2$SO$_4$ solution with a volume ratio of 100: 5:1, a remarkable increase (nearly 10 times to ~85.5 μA/cm^2) in photocurrent density was obtained (Figure 4b). This indicates that H$_2$SO$_4$ plays an important role in improving the conductivity and supporting the protons of the electrolyte [30]. On the other hand, a slight decrease in the photocurrent of the MAPbI$_3$/Au is obtained in the sequence runs, which could be attribute to the degradation of the sample. Thus, protective engineering should be developed to improve the stability of the MAPbI$_3$/Au in ethanol/H$_2$O/H$_2$SO$_4$ solution. Based on the above results, the MAPbI$_3$/Au a promising platform for enhancing solar hydrogen evolution.

The mechanism of the PECR on MAPbI$_3$/Au is proposed as shown in Figure 4c. When the MAPbI$_3$/Au film is irradiated with visible light, electrons (e$^-$) in the valence band (VB) were excited and transferred to the conduction band (CB) of MAPbI$_3$, leaving holes (h$^+$) in the VB. Then, driven by the potential differences between the CB of the MAPbI$_3$ (-3.9 eV vs AVS) and the work function of Au (-5.1 eV vs AVS), the photogenerated electrons on the CB of MAPbI$_3$ transferred to the surface of Au in which H$_2$ generation take place. The holes transferred from the MAPbI$_3$ to the counter electrode.

2.3 Theoretical calculations

The electrical interaction between H$_2$O and perovskite surfaces is of great importance

in photocatalysed H_2O splitting reactions. Therefore, it is necessary to unveil the surface interaction between H_2O and $MAPbI_3$ for photocatalysis. Here we start with the first-principles density functional theory (DFT) calculations to describe the atomic and electronic structures of $MAPbI_3$ in photocatalystic systems. The details for the atomic structures of $MAPbI_3$ are shown in Figure S6. According to the experimental results of TEM combined with XRD, the (110) surface is dominating in the prepared $MAPbI_3$ sample, while the (001) surface is also found to be stable in other experiments [31]. They are both considered in the simulation with PbI- and MAI-terminated surfaces. The density of states for PbI-terminated (110) and (001) surfaces has been studied by Haruyama *et al* [32]. Calculated bandgaps for (001-PbI) and (110-PbI) surfaces in their work were 1.56 eV and 1.63 eV, respectively without spin orbit coupling (SOC). While the SOC is implemented, the bandgaps were changed to 0.76 eV and 0.68 eV, respectively. We also calculated bandgaps for both PbI- and MAI-terminated surfaces as indicated in Table 1. Calculated bandgaps without SOC are much smaller than in Haruyama's results, while those with SOC are more comparable. The difference may be caused by the change of pseudopotential and/or lattice parameters.

Table 1. Calculated bandgap with and without SOC. The unit of energy is eV.

Surfaces	w/o SOC	with SOC
001-MAI	1.73	0.96
110-MAI	1.51	0.88
001-PbI	1.06	0.56
110-PbI	1.00	0.40

In our results, bandgaps for MAI-terminated surfaces are much larger than for the PbI-terminated surfaces. The reason is that the loose-packed MAI-terminated surface

weakens the interaction between the I atoms on the surface, leading to less dispersion of valance bands, including SOC cutting down the bandgap by half, as the SOC modifies the shape of Pb orbitals, as mentioned in previous reports [33]. However, experimental results show that the studied perovskite has a bandgap of 1.62 eV (corresponding to the PL peak located at 765 nm in this work), which is much larger than the calculated bandgaps with SOC included in this work. The reason why the consistency is better without SOC is actually easy to understand. PBE functional used in our calculation usually underestimates the bandgap, while excluding SOC will enlarge the gap. These effects cancel each other and make the PBE result without SOC more close to the experimental result. Therefore, later discussion is conducted without SOC. Comparing the theoretical and the experimental results (bandgap of 1.62 eV from the PL peak and preferred growth plane of (110) from XRD patterns), the sample is probably terminated by 110-MAI layers in this work.

However, the interaction between H_2O and the surface atoms of $MAPbI_3$ is of great importance to the proposed photocatalytic H_2 production as shown in Figure 4. The most stable adsorption structure is shown in Figure S7. The H_2O molecule adsorbs on the short bridge site between I atoms on MAI-terminated surfaces, with its H atoms pointing towards I atoms nearby, while the molecule sits on the top site of Pb on PbI-terminated surfaces. Adsorption energies for single H_2O molecules are -0.42 eV (001-MAI), -0.50 eV (110-MAI), -0.61 eV (001-PbI) and -0.55 eV (110-PbI), indicating van der Waals dominated interactions between molecule and target sample. Since H_2O is a polar molecule, its orientation on the surface is stabilized by the local dipole formed by

Pb^{2+} and I^-. Partial density of states for surface I and/or Pb atoms and adsorbed H_2O molecules are shown in Figure 5a. The hybridization between orbitals of H_2O and MAI-terminated surfaces is very weak since the H_2O-surface interaction is mainly composed of H-I interactions. Generating photocurrent on MAI-terminated surfaces is possible, but it is not likely to transfer an electron from the MAI-terminated substrate to H_2O, although these surfaces are indicated by bandgap calculation. On the other hand, O atoms are close to Pb atoms on PbI-terminated surfaces, strengthening the H_2O-surface interaction. There are several hybridization molecular orbitals (*h*-MO) in the region of 2~3 eV above the valance band maximum, indicating stronger interactions between H_2O orbitals and the conductance band of $MAPbI_3$. The real-space projections of the wavefunction for the valance band of PbI-terminated surfaces and the marked *h*-MO are plotted in Figures 5 (b)-(e). Valance bands are mainly composed of Pb-s and I-p orbitals, while *h*-MO states are composed of O-p and Pb-p orbitals. It is possible to excite an electron from a valance band to a conduction band and then to the molecular orbital of H_2O via Xe lamp. Therefore, PbI-terminated surfaces are better to generate H_2 and the outmost surface should be tuned via changing the growth environment [25] although the MAI-terminated surface possess a similarly calculated bandgap to that of the experiment. It should be noted here that we cannot model the complex system containing H_2O, perovskite and Au at the same time due to the limitation of computational effort. Therefore, we made a compromise via modeling the interface interaction between Au and perovskite. Results collected in Figure S8 & S9 showed that adding Au-layers to the perovskite surface introduced a few new states to the
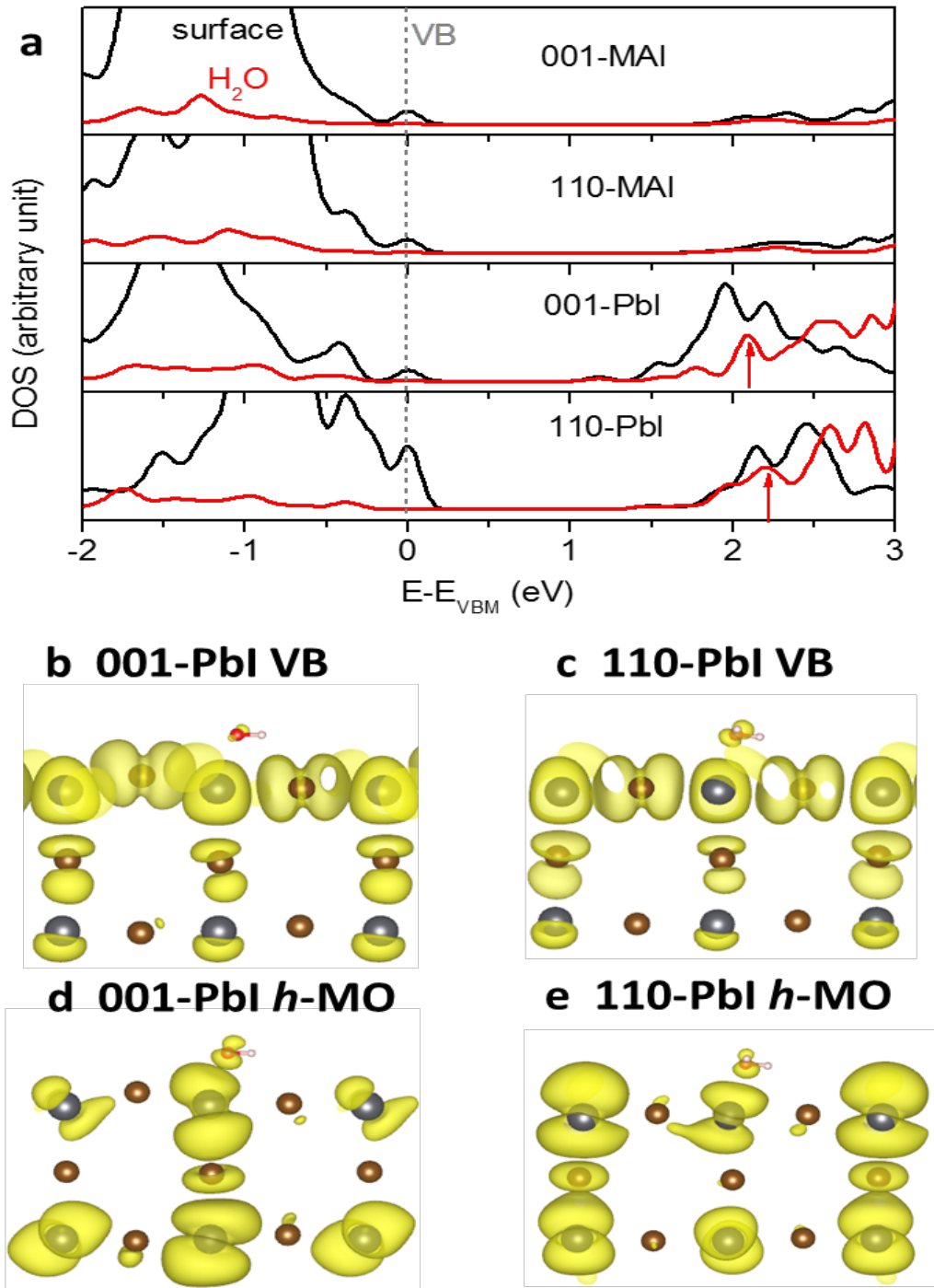
Figure 5. Partial density of states for MAPbI$_3$ surfaces and real-space projection of wavefunctions.　(a)

Density of states for adsorbed H_2O (red) and surface atoms (black). Red arrows point to the hybridized molecular orbital (*h*-MO) of H_2O. Energies are shifted with respect to the valance band maximum. DOS for H_2O are amplified for better contrast. (b)-(e) Real-space projection of the wavefunction for the valance bands and *h*-MO. The value for the plotted isosurface is 0.0002 *e*/Bohr.

Accordingly, the simulations reveal the MAPbI$_3$ perovskite crystals have potential application in the photocatalytic system. The bandgap of the MAPbI$_3$ is in agreement with the calculated results of a 110-MAI terminated surface in this work but different from 110-PbI terminated surface in reference 25, which may be induced by the change of pseudopotential and/or lattice parameters. However, the simulated results for the interaction between H_2O and the surface atoms of the MAPbI$_3$ are playing important roles in the photocatalytic system.

3. Conclusion

In summary, the MAPbI$_3$ crystals can effectively perform PECRs. The photocurrent of the MAPbI$_3$ could be remarkably increased by the deposition of a Au film on the top of the perovskite, and the highest photocurrent density could be up to 85.5 $\mu A/cm^2$ in H_2SO_4 system. Combining the experiments with the simulation results, we can find the strong interaction between H_2O orbitals and the conductance band of MAPbI$_3$, revealing the potential of MAPbI$_3$/Au for efficiency PECR. Our study presents the first successful preparation of large-area PVD-perovskite-based photo-electrochemical reaction material—a critical advancement in controlled production of MAPbI$_3$/Au junction for investigating the feasibility of integrating MAPbI$_3$ into photocatalytic

systems.

4. Materials and Methods

4.1 Preparation of Lead Halide crystal: The PbI_2 crystals were grown via an atmospheric pressure physical vapor deposition (APPVD) method. In brief, PbI_2 powder (99%, Sigma-Aldrich) was put in a ceramic boat and placed at the center of a 1-inch in diameter quartz tube mounted on a single-zone furnace. Then the fluorine doped tin oxide (FTO) coated glass substrates were placed into the down-stream region of the furnace (as shown in Figure S1). The growth temperature of the PbI_2 plates on FTO was 385 °C and the growth time was in a range of 5 - 20 h. The PbI_2 crystals can also grow directly on a copper grid under the same conditions, for transmission electron microscopy (TEM) observations.

4.2 Synthesis of Perovskites (MAPbI₃): Methylammonium iodide (CH_3NH_3I) powder (99%, Sigma-Aldrich) was placed upstream in a quartz tube and the FTO/glass substrates (also the TEM grids) coated with the PbI_2 crystals were placed 9 to 10 cm away from the powder. Before the reaction, the furnace was purged by the carrier gas (argon) for 5 - 10 min to remove the residual air. Then the reaction was carried out at atmospheric pressure with an argon gas flow rate of 45 sccm (standard cubic centimeters per minute) for several hours. The temperature at the CH_3NH_3I source region was at 160 °C. The conversion area at the substrate region could be up to 4 – 5 cm along the substrate. Finally, the furnace was naturally cooled down to room temperature. The gold films with a thickness of 50 nm were deposited onto the surface of the perovskite crystals in a thermal evaporation system.

4.3 Materials characterizations: Raman spectra were collected using a Horiba Jobin Yvon HR800 Raman microscopic system equipped with a 488 nm laser operating at 180 mW. The spot size of the excitation laser is ∼1 μm. The atomic force microscopy (AFM) measurements were performed in a Veeco Dimension-Icon system with a scanning rate of 0.972 Hz. The PL measurement was carried out using an excitation laser of 488 nm. The structural properties of the PbI_2 and $MAPbI_3$ samples were characterized by a Jeol JEM-2100F scanning transmission electron microscope (STEM) and energy dispersive X-ray (EDX) operating at 200 kV. The morphologies of the PbI_2 and $MAPbI_3$ were observed by a Leica Stereoscan 440 scanning electron microscope (SEM). X-ray diffraction (XRD) was carried out with a Rigaku SmartLab X-ray diffractometer (Cu K_α radiation $\lambda = 1.54056$ Å) operating at 45 kV and 200 mA. The UV-vis spectra were recorded at room temperature on a Shimadzu UV-2550 UV-vis spectrophotometer.

4.4 Characterization of MAPbI₃-based photocatalyst: The photocurrent density of the sample was measured in the presence of ethanol, ethanol/H_2O solution and ethanol/H_2SO_4 solution. Here we used the as-prepared film as the working electrode, Ag/AgCl as the reference electrode and Pt wire as the counter electrode. Photocurrent densities were measured using a potentiostat (CHI 660E Instruments) with a constant potential (0 V or -0.5 V vs. Ag/AgCl) and under a 300 W Xe lamp with a cut-off filter ($\lambda > 420$ nm) irradiation at 100 mWcm^{-2} (PLS-SXE 300, Beijing Trusttech Co. Ltd, China).

4.5 DFT calculations: Calculations were performed using the Perdue-Burke-Enzerhof

(PBE) functional for the exchange-correlation functional [19], the projector augmented method [20, 21] and a plane-wave basis set as implemented in the Vienna ab-initio simulation package [22, 23]. A semi-empirical dispersion correction (DFT-D3) generated by Grimme *et al* was used in the simulation [24]. Energy cut-off for the plane-wave basis was set to 400 eV, which was increased to 500 eV in static calculations. DFT simulations were conducted for tetragonal $MAPbI_3$. The optimized lattice parameters for the bulk phase were $a = 8.650$ Å and $c = 12.744$ Å, close to the experimental values ($a = 8.809$ Å, c = 12.744 Å) [25]. Both the (001) and (110) surfaces of the tetragonal lattice are nonpolar surfaces stacked by MAI and PbI_2 planes. Two types of terminations (PbI and MAI) were considered. Those surfaces are named as 001-MAI, 110-MAI, 001-PbI and 110-PbI respectively. Symmetric slab models were used to avoid the unrealistic dipole. The slabs were thicker than 15 Å, separated by vacuum space of 20 Å. The first Brillouin zone of the supercell was sampled by a $3 \times 3 \times 1$ k-mesh. All atoms except for the bottom layer were fully relaxed until the residual force for each atom was less than 0.02 eV/Å. Relaxed slab models for these surfaces are shown in Figure S6. The positions of surface atoms changed due to surface relaxation, while the displacements for atoms in the middle layer are less than 0.2 Å. It proves that our slab models are thick enough to avoid the interaction between top and bottom surfaces.

Acknowledgements

Reference

[1] W. Wang, M. O. Tadé, Z. Shao. **Research progress of perovskite materials in photocatalysis- and photovoltaics-related energy conversion and environmental treatment.** *Chem. Soc. Rev.* 44 (2015) 5371.

[2] M. A. Green, A. Ho-Baillie, H. J. Snaith. **The emergence of perovskite solar cells**. *Nat. Photonics* 8 (2014) 506−514.

[3] J. H. Heo, S. H. Im, J. H. Noh, T. N. Mandal, C. S. Lim, J. A. Chang, Y. H. Lee, H.-j. Kim, A. Sarkar. **Efficient inorganic-organic hybrid heterojunction solar cells containing perovskite compound and polymeric hole conductors**. *Nat. Photonics* 7 (2013) 486−491.

[4] J. Burschka, N. Pellet, S. J. Moon, R. Humphry-Baker, P. Gao, M. K. Nazeeruddin, M. Gratzel. **Sequential deposition as a route to high-performance perovskite-sensitized solar cells.** *Nature* 499 (2013) 316−319.

[5] Lee, M. M. et al. Efficient Hybrid Solar Cells Based on Meso-Superstructured Organometal Halide Perovskites. Science 338, 643 (2012).

[6] O. Ergen, S. M. Gilbert, T. Pham, S. J. Turner, M. T. Z. Tan, M. A. Worsley, A. Zettl. **Graded bandgap perovskite solar cells**. *Nature Materials* 16 (2017) 522–525.

[7] M. Liu, M. B. Johnston, H. J. Snaith. **Efficient planar heterojunction perovskite solar cells by vapour**. *Nature* 501 (2013) 395.

[8] J. H. Heo, S. Im, J. Noh, T. N. Mandal, C. Lim, J. Chang, Y. Lee, H. Kim, A. Sarkar, Md. K. Nazeeruddin, M. Grätzel, S. Seok. **Efficient inorganic–organic hybrid heterojunction solar cells containing perovskite compound and polymeric hole**

conductors. *Nat. Photonics* 7 (2013) 486.

[9] A. Kojima, K. Teshima, Y. Shirai, T. Miyasaka. **Organometal halide perovskites as visible-light sensitizers for photovoltaic cells.** *J. Am. Chem. Soc.* 131 (2009) 6050.

[10] J. H. Noh, S. Im, J. Heo, T. N. Mandal, S. Seok. **Chemical Management for Colorful, Efficient, and Stable Inorganic–Organic Hybrid Nanostructured Solar Cells.** *Nano Lett.* 13 (2013) 1764.

[11] L. Etgar, P. Gao, Z. Xue, Q. Peng, A. K. Chandiran, B. Liu, Md. K. Nazeeruddin, M. Grätzel. **Mesoscopic CH$_3$NH$_3$PbI$_3$/TiO$_2$ Heterojunction Solar Cells**. *J. Am. Chem. Soc.* 134 (2012) 17396.

[12] B. Cai, Y. Xing, Z. Yang, W. Zhang, J. Qiu. **High performance hybrid solar cells sensitized by organolead halide perovskites.** *Energy Environ. Sci.* 6 (2013) 1480.

[13] J. Im, I. Jang, N. Pellet, M. Grätzel, N. Park. **Growth of CH$_3$NH$_3$PbI$_3$ cuboids with controlled size for high-efficiency perovskite solar cells.** *Nat. Nanotechnol.* 9 (2014) 927-932.

[14] Q. Dong, Y. Fang, Y. Shao, P. Mulligan, J. Qiu, L. Cao, J. Huang. **Solar cells. Electron-hole diffusion lengths > 175 μm in solution-grown CH$_3$NH$_3$PbI$_3$ single crystals.** *Science* 347 (2015) 967.

[15] S. Ha, X. Liu, Q. Zhang, D. Giovanni, T. Sum, Q. Xiong. **Synthesis of Organic– Inorganic Lead Halide Perovskite Nanoplatelets: Towards High-Performance Perovskite Solar Cells and Optoelectronic Devices.** *Adv. Optical Mater.* 2 (2014) 838–844.

[16] L. Niu, X. Liu, C. Cong, C. Wu, D. Wu, T. Chang, H. Wang, Q. Zeng, J. Zhou, X.

Wang, W. Fu, P. Yu, Q. Fu, S. Najmaei, Z. Zhang, B. Yakobson, B. Tay, W. Zhou, H. Jeng, H. Lin, T. Sum, C. Jin, H. He, T. Yu, Z. Liu. **Controlled Synthesis of Organic/Inorganic van der Waals Solid for Tunable Light–Matter Interactions.** *Adv. Mater.* 27 (2015) 7800–7808.

[17] S. Park, W. Chang, C. Lee, S. Park, H. Ahn, K. Nam. **Photocatalytic hydrogen generation from hydriodic acid using methylammonium lead iodide in dynamic equilibrium with aqueous solution**. *Nat. Energy* 2 (2016) 16185.

[18] G. Wang, D, Li, H. Cheng, Y. Li, C. Chen, A. Yin, Z. Zhao, Z. Lin, H. Wu, Q. He, M. Ding, Y. Liu, Y. Huang, X. Duan. **Wafer-scale growth of large arrays of perovskite microplate crystals for functional electronics and optoelectronics**. *Sci. Adv.* 1 (2015) e1500613.

[19] J. P. Perdew, K. Burke, M. Ernzerhof. **Generalized Gradient Approximation Made Simple**. *Phys. Rev. Lett.* 77 (1996) 3865–3868.

[20] P. E. Blöchl. **Projector augmented-wave method**. *Phys. Rev. B* 50 (1994) 17953–17979.

[21] G. Kresse. **From ultrasoft pseudopotentials to the projector augmented-wave method**. *Phys. Rev. B* 59 (1999) 1758–1775.

[22] G. Kresse, J. Furthmüller. **Efficiency of ab-initio total energy calculations for metals and semiconductors using a plane-wave basis set**. *Comput. Mater. Sci.* 6 (1996) 15–50.

[23] G. Kresse, J. Furthmüller. **Efficient iterative schemes for *ab initio* total-energy calculations using a plane-wave basis set**. *Phys. Rev. B* 54, 11169–11186 (1996).

[24] S. Grimme, J. Antony, S. Ehrlich, H. Krieg. **A consistent and accurate *ab initio* parametrization of density functional dispersion correction (DFT-D) for the 94 elements H-Pu.** *J. Chem. Phys.* 132 (2010) 154104.

[25] Y. Kawamura, H. Mashiyama, K. Hasebe. **Structural Study on Cubic–Tetragonal Transition of CH₃NH₃PbI₃.** *J. Phys. Soc. Japan* 71 (2002) 1694–1697.

[26] P. Luo, Z. Liu, W. Xia, C. Yuan, J. Cheng, Y. Lu. **A simple *in situ* tubular chemical vapor deposition processing of large-scale efficient perovskite solar cells and the research on their novel roll-over phenomenon in *J–V* curves.** *J. Mater. Chem. A* 3 (2015) 12443-12451.

[27] C. Quarti, G. Grancini, E. Mosconi, P. Bruno, J. M. Ball, M. M. Lee, H. J. Snaith, A. Petrozza, F. De Angelis. **The Raman Spectrum of the CH₃NH₃PbI₃ Hybrid Perovskite: Interplay of Theory and Experiment.** *J. Phys. Chem. Lett.* 5 (2014) 279–284.

[28] Q. Chen, H. Zhou, Z. Hong, S. Luo, H. Duan, H. Wang, Y. Liu, G. Li, Y. Yang. **Planar Heterojunction Perovskite Solar Cells via Vapor-Assisted Solution Process.** *J. Am. Chem. Soc.* 136 (2014) 622-625.

[29] T. Baikie, Y. Fang, J. M. Kadro, M. Schreyer, F. Wei, S. G. Mhaisalkar, M. Graetzeld, T. J. Whitec. **Synthesis and crystal chemistry of the hybrid perovskite (CH₃NH₃)PbI₃ for solid-state sensitised solar cell applications.** *J. Mater. Chem. A* 1 (2013) 5628-5641.

[30] M. Wang, L. Chen, L. Sun. **Recent progress in electrochemical hydrogen production with earth-abundant metal complexes as catalysts.** *Energy. Environ. Sci.*

5 (2012) 6763-6778.

[31] L. She, M. Liu, D. Zhong. **Atomic Structures of CH$_3$NH$_3$PbI$_3$ (001) Surfaces.** *ACS nano* 10 (2016) 1126-1131.

[32] J. Haruyama, K. Sodeyama, L. Han, Y. Tateyama. **Termination Dependence of Tetragonal CH$_3$NH$_3$PbI$_3$ Surfaces for Perovskite Solar Cells.** *J. Phys. Chem. Lett.* 5 (2014) 2903-2909.

[33] J. Even, L. Pedesseau, J. Jancu, C. Katan. **Importance of Spin–Orbit Coupling in Hybrid Organic/Inorganic Perovskites for Photovoltaic Applications.** *J. Phys. Chem. Lett.* 4 (2013) 2999-3005.